

Shallow Megathrust Rupture during the 10 February 2021 M_w 7.7 Southeast Loyalty Islands Earthquake Sequence

Lingling Ye¹, Wenzheng Gong¹, Thorne Lay², Hiroo Kanamori³, and Xiaofei Chen¹

Abstract

On 10 February 2021, an M_w 7.7 thrust earthquake ruptured the megathrust along the southeast Loyalty Islands within the strong bend in the plate boundary between the Australian plate and the North Fiji basin. The mainshock involved rupture with ~ 50 s duration, with pure thrust slip concentrated in an east–west-trending slip patch with up to 4.2 m of slip extending from 10 to 25 km depth. Slip at depths < 10 km is negligible on the curved fault surface, which conforms to the SLAB2 interface model. Static stress-drop estimates are ~ 5.5 MPa, and the radiated energy is 2.38×10^{15} J, with the moment-scaled value of 5.7×10^{-6} . The relatively shallow rupture from 10 to 25 km was moderately efficient in generating tsunami, with waves amplitudes up to 20 cm recorded in New Caledonia, New Zealand, Kermadec, and Fiji. Numerous $M5+$ normal-faulting aftershocks occur south of the trench, indicating effective stress change transfer from the megathrust to the bending flange of the Australian plate that is negotiating the bend in the trench. Highly productive sequences involving paired thrust and normal faulting have repeatedly occurred westward along the northwest-trending portion of the Loyalty Islands region, also indicating unusually efficient stress communication.

Cite this article as Ye, L., Gong, W., Lay, T., Kanamori, H., and Chen, X. (2021). Shallow Megathrust Rupture during the 10 February 2021 M_w 7.7 Southeast Loyalty Islands Earthquake Sequence, *The Seismic Record*, **1**(3), 154–163, doi: [10.1785/0320210035](https://doi.org/10.1785/0320210035).

Introduction

The Vanuatu (New Hebrides) subduction zone extending from about 10.5° S near the Santa Cruz Islands to about 23° S southeast of the Loyalty Islands is a seismically active arc with the Australian plate underthrusting the Pacific plate and the western and southern North Fiji basin microplates (e.g., Louat and Pelletier, 1989; Fig. 1). The arc is laterally bounded by strong corner bends, with transforms connecting to the Solomon Islands in the north and to a seismic line south of Fiji in the south. The northern Vanuatu subduction zone has experienced larger historical earthquakes than the southernmost portion (McCann *et al.*, 1979; Nishenko, 1991; Cleveland *et al.*, 2014), with the most recent being the great M_w 8.0 event of 6 February 2013 near the Santa Cruz Islands (Lay *et al.*, 2013; Cleveland *et al.*, 2014; Hayes *et al.*, 2014). Large earthquake doublets and triplets have occurred both in northern Vanuatu and the Loyalty Islands region,

indicating strong stress change interactions along the megathrust plate boundary (e.g., Cleveland *et al.*, 2014).

The southern bend in the subduction zone near the Loyalty Islands intrinsically involves complex tearing and deformation of the underthrusting Australian plate, with arc-normal thrusting occurring all along the $\sim 70^\circ$ bend in the zone. This curved geometry is accommodated by tearing the underthrusting

1. Department of Earth and Space Sciences, Southern University of Science and Technology, Shenzhen, Guangdong, China, <https://orcid.org/0000-0001-9689-4149> (LY); <https://orcid.org/0000-0001-6078-3498> (WG); <https://orcid.org/0000-0002-0950-8121> (XC);
2. Department of Earth and Planetary Sciences, University of California Santa Cruz, Santa Cruz, California, U.S.A., <https://orcid.org/0000-0003-2360-4213> (TL);
3. Seismological Laboratory, California Institute of Technology, Pasadena, California, U.S.A., <https://orcid.org/0000-0001-8219-9428> (HK)

*Corresponding author: yell@sustech.edu.cn

© 2021. The Authors. This is an open access article distributed under the terms of the CC-BY license, which permits unrestricted use, distribution, and reproduction in any medium, provided the original work is properly cited.

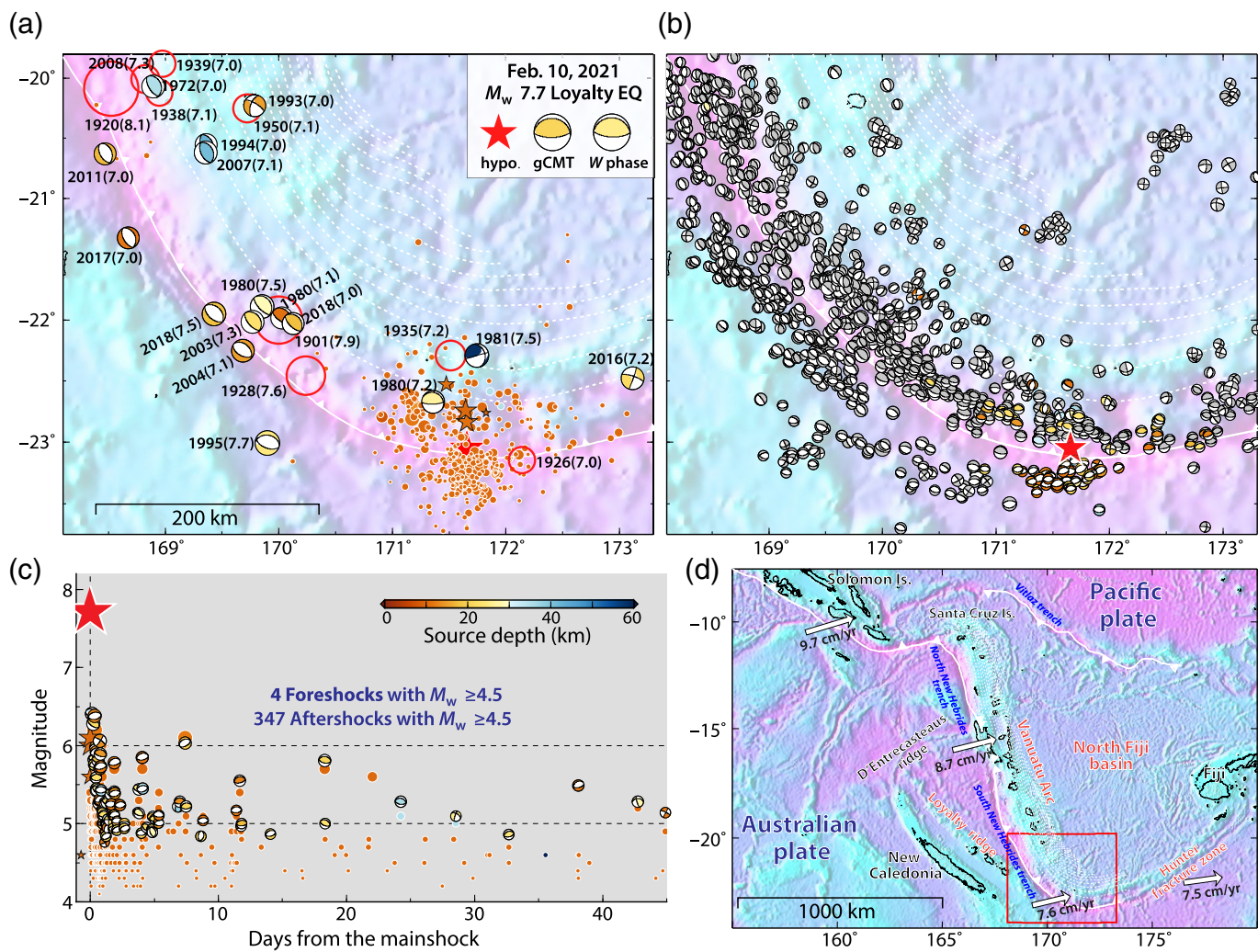


Figure 1. The 2021 southeast Loyalty Islands earthquake sequence relative to background seismicity in the southern Vanuatu subduction zone. (a) U.S. Geological Survey National Earthquake Information Center (USGS-NEIC) locations for foreshocks (brown stars) and aftershocks (dots) in the first 45 days with magnitude ≥ 4.5 , with historical shallow (≤ 70 km) events larger than M_w 7.0 labeled by year and magnitude from USGS-NEIC catalog from 1900 to 1976 (red circles) and from Global Centroid Moment Tensor (Global CMT) catalog since 1976 (focal mechanisms). Foreshocks, aftershocks, and focal mechanisms are color-coded by the source depth (see panel c). The white-dashed curves denote the slab interface depth from model SLAB2 in 20 km increments (Hayes *et al.*, 2018), and the toothed curve indicates the position of the trench. (b) Focal mechanisms for all shallow (≤ 70 km) events from the Global CMT catalog for 1976 with historical events in gray and aftershocks color-coded by the source depth (see panel c), respectively. (c) Time sequence plot for foreshocks and aftershocks with magnitude ≥ 4.5 . (d) Tectonic setting for the Loyalty Islands earthquake sequences. White arrows show relative plate motions with respect to the Pacific plate from the MORVEL model (DeMets *et al.*, 2010). The red box indicates the study area in panels (a) and (b).

plate, with an underthrust flange along the eastern extension sustaining convergence as there is a transition to strike-slip faulting to the east (e.g., Monzier *et al.*, 1984; Lister *et al.*, 2012). Strike-slip shearing deformation within the overriding southern North Fiji basin block appears to help accommodate the progressive slip partitioning around the bend (Louat and Pelletier, 1989). Observations from the Global Positioning System along the Vanuatu archipelago and the Loyalty Islands (e.g., Calmant *et al.*, 2003) show variable convergence along the western North Fiji basin complicated by deformation and segmentation into blocks within the overriding plate. In the southern region, the incoming plate has significant bathymetric relief, with the Loyalty ridge impinging on the subduction zone.

This region has a substantial history of major earthquakes (Fig. 1a), with magnitude as large as M_w 7.7, but no history of

great ($M_w \geq 8$) earthquakes. The convergence rate is high, ~ 8 cm/yr, and the background seismicity is correspondingly high, but the region is distinct in having an unusual amount of activity seaward of the trench. Large earthquakes in this region are accompanied by highly productive aftershock sequences. Numerous sequences of large historic ruptures along the southern Vanuatu arc and the Loyalty Islands (Fig. 1a) show strong interactions between the megathrust and the intraplate environment seaward of the trench. The 1995 M_w 7.7, 2004 M_w 7.1, and 2018 M_w 7.5 events west of the trench all involve normal faulting, whereas the 1980 M_w 7.5, 2003 M_w 7.3, and 2018 M_w 7.1 events all involve thrust faulting. The 1980 M_w 7.5 event was part of a sequence of M_w 6.5–7.5 thrust events (Vidale and Kanamori, 1983), and the 1995 M_w 7.7 event was an isolated normal faulting event relatively far seaward of the trench, whereas the 2003–2004 and 2018 events are doublets, closely spaced in time and location.

On 10 February 2021, the plate boundary southeast of the Loyalty Islands experienced a major thrusting earthquake with M_w 7.7 (13:19:55.53 UTC, 23.051° S, 171.657° E, 10.0 km deep; U.S. Geological Survey National Earthquake Information Center [USGS-NEIC]) (Fig. 1a). The earthquake sequence was very productive, including three large thrusting foreshocks with M_w from 5.6 to 6.1 within 1 hr before the mainshock and 347 aftershocks larger than M_w 4.5 in the first 45 days after the event (Fig. 1c; Ye *et al.*, 2020; Fan *et al.*, 2021). We analyze the rupture process of the mainshock using global broadband seismic recordings and consider the 2021 sequence relative to other sequences that have occurred along the Loyalty Islands.

Point-Source Mechanisms

The 10 February 2021 M_w 7.7 southeast Loyalty Islands mainshock involved thrust faulting on a northward dipping fault with a strike close to east–west, centered in the strongly curved plate boundary between the Australian plate and southern North Fiji basin. The USGS-NEIC *W*-phase inversion has a predominantly double-couple solution with strike $\phi = 246^\circ$, dip $\delta = 17^\circ$, rake $\lambda = 65^\circ$, and a seismic moment $M_0 = 4.364 \times 10^{20}$ N · m (M_{ww} 7.69). The centroid depth is 25.5 km. The Global Centroid Moment Tensor (Global CMT) solution, based on a dataset of 467 body waves, 517 mantle waves, and 440 surface waves low-pass filtered at periods of 50, 150, and 50 s, respectively, has a best double couple with $\phi = 277^\circ$, $\delta = 22^\circ$, $\lambda = 98^\circ$, $M_0 = 4.12 \times 10^{20}$ N · m (M_w 7.7), centroid depth 21.0 km, and 28.5 s centroid time shift. Given the relatively large differences in strike and rake between these routine solutions, we

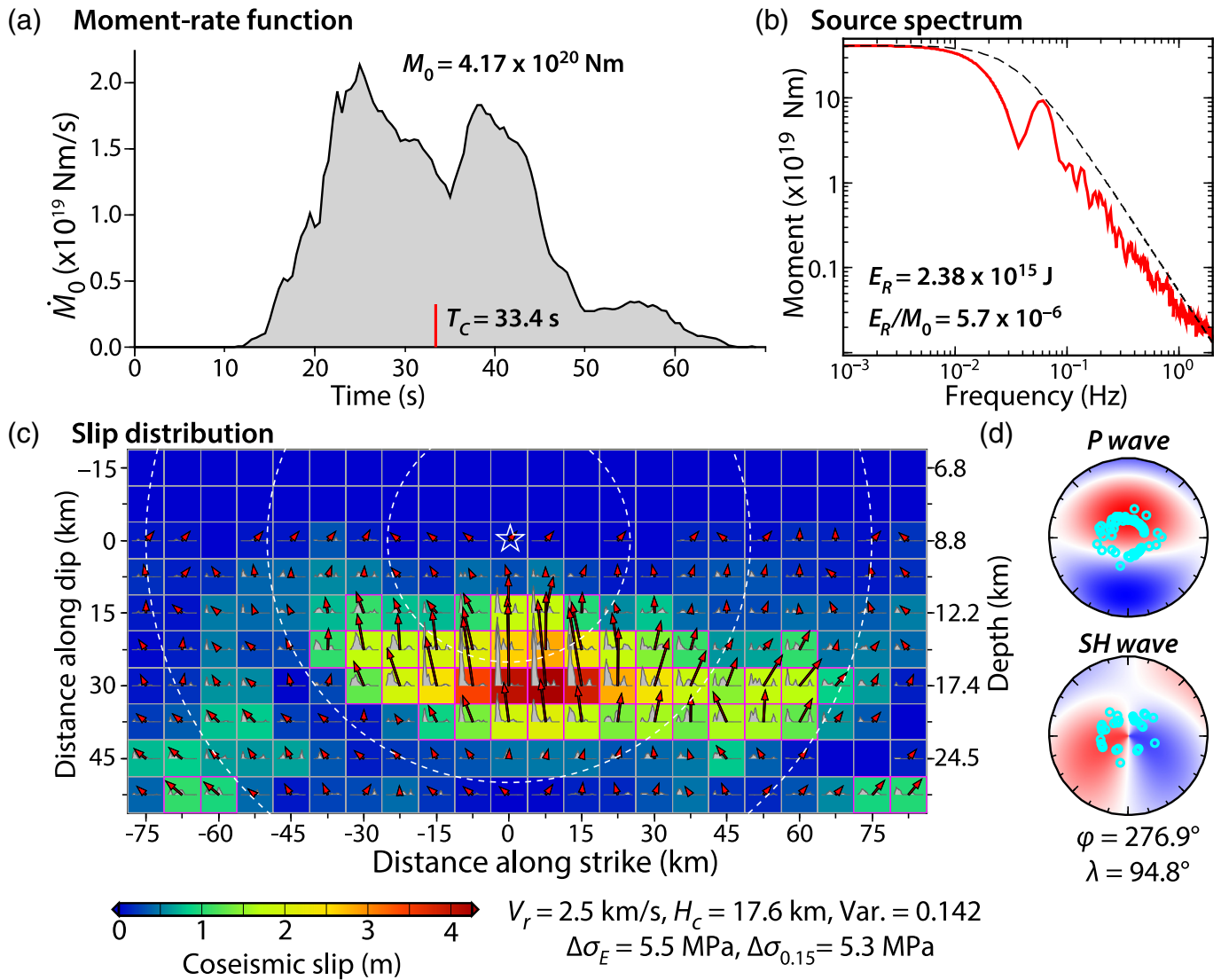
performed our own *W*-phase inversion (Kanamori and Rivera, 2008) using 145 ground-motion channels from 79 stations filtered in the passband 0.002–0.005 Hz. We carefully screened the data quality and checked the waveform predictions. This inversion gives a centroid depth of 25.5 km, the best double couple having $\phi = 276.9^\circ$, $\delta = 21.2^\circ$, $\lambda = 94.8^\circ$, $M_0 = 4.15 \times 10^{20}$ N · m (M_w 7.68), and a 27 s centroid time shift, which is very similar to the Global CMT solution.

Finite-Fault Slip Model for the Mainshock

The USGS computed an initial planar finite-fault solution for the M_w 7.7 southeast Loyalty Islands event using teleseismic body and surface waves, assuming a strike of 264° and a dip of 19° . The result is a concentrated slip patch at depths less than 10 km with slip of up to 6 m. In our own preliminary inversions of teleseismic body waves following the procedure of Ye, Lay, *et al.* (2016) for planar megathrust faults with uniform dip angles ranging from 21° to 23° using teleseismic body waves, we found slip patches near 20 and 10 km depth, respectively. Given that uniform dip extending to very shallow depth is unlikely, we conduct inversions of teleseismic body waves for a 2.5D fault surface, which varies in dip with depth along the fault, guided by the SLAB2 plate interface model (Hayes *et al.*, 2018), along with variable bathymetry above the fault (Ye, Kanamori, *et al.*, 2016), as there are only minor variations along strike over ~ 100 km. This model has a strike of 276.9° , and the dip increases from 5° near the trench to 37° near 30 km depth (Figs. 2 and 3). The water depth varies from 6.0 km near the trench to 1.1 km above the down-dip edge of the model (Fig. 3).

The seismic waveform data used for the inversion are 70 *P* waves and 33 *SH* waves from global broadband seismic stations in the distance range of 30° – 95° with good azimuthal distribution (Figs. 2d and 4). The raw seismic waveform recordings are corrected by removing instrument response to ground displacement bandpass filtered in the frequency band of 0.005–0.9 Hz. We align the traces on very weak initial arrivals consistent with the USGS-NEIC origin, with there being about 10 s before strong arrivals that are captured in the inversion.

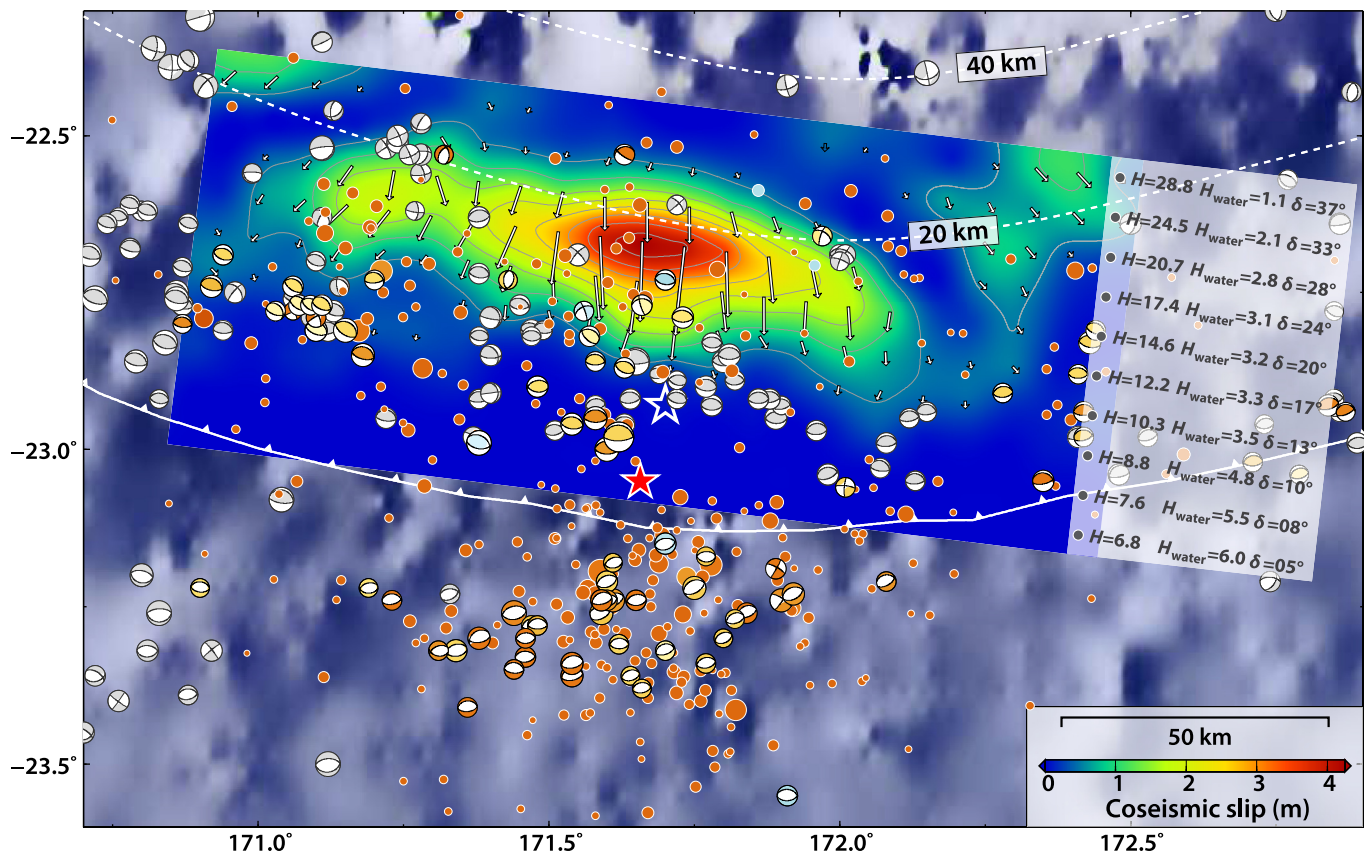
We apply a least-squares kinematic inversion with multiple rake-varying ($\pm 45^\circ$ from a reference value given by our *W*-phase inversion) subfault source time function windows (e.g., Hartzell and Heaton, 1983; Kikuchi and Kanamori, 1991; Ye, Lay, *et al.*, 2016) to determine the space-time slip distribution for the M_w 7.7 event using the 2.5D dip-varying fault grid (Figs. 2 and 3). Model Crust 1.0 (Laske *et al.*, 2013) was used for the local source velocity structure, adapted to have



variable bathymetry over the fault. Local 1D Green's functions are used for each row of the fault, approximating the far-field P and SH response for the 2.5D structure.

For our preferred model, the grid has $22.75 \text{ km} \times 7.5 \text{ km}$ subfault columns along strike and 10 rows along dip, with the subfault source time functions being represented by 12 2.0 s rise time-symmetric triangles, with 2.0 s time shift between triangles, giving maximum possible subfault duration of 26 s . An upper bound of 2.5 km/s was imposed for the rupture speed. A hypocenter at 22.93° S , 171.7° E , 8.8 km depth was assumed to reconcile the USGS-NEIC epicenter with the 2.5D fault grid (blue star in Fig. 3). The result of the 2.5D inversion of seismic data is shown in Figure 2, with seismic moment, $M_0 = 4.17 \times 10^{20} \text{ N} \cdot \text{m}$ (M_w 7.68), and a slip centroid depth of 17.6 km . Peak slip of about 4.2 m is found in a concentrated slip patch

Figure 2. Source model obtained from inversion of teleseismic body waves for the M_w 7.7 mainshock. (a) Moment-rate function indicating the seismic moment M_0 and centroid time T_C . (b) Source spectrum obtained from the moment-rate function for frequencies less than 0.05 Hz and from stacks of radiation pattern and propagation corrected far-field P -wave spectra for higher frequencies. E_R is the radiated seismic energy up to 1 Hz . (c) Spatial distribution of slip on the 2.5D fault model (see map position in Fig. 3). The slip in each fault is indicated by the color scale with red vectors showing the slip magnitude and direction (zero slip for those grids without vector), and the gray polygons indicating the subfault source time functions (parameterized as 12 2.0 s rise time-symmetric triangles offset by 2.0 s). White-dashed circles indicate the position of the rupture front in 10 s intervals. The white star shows the hypocentral location. (d) Lower hemisphere focal mechanism plots showing the distribution of data used in the inversion and the P and SH radiation patterns. The variance reduction of waveform fitting for this model is 0.142 , and waveform predictions are shown in Figure 4.



that extends bilaterally over ~ 100 km along strike. The moment rate function commences about 12 s after the origin time, with unresolved early slip, and then has about 50 s duration, with two peaks at around 25 and 35 s into the rupture originating from the bilateral growth of the slip zone. We find almost no slip at depths shallower than 10 km, when we used the more realistic interplate geometry. The radiated energy E_R estimated from the moment-rate function for periods longer than 20 s and from the average of propagation-corrected broadband P waves for periods from 20 to 1 s is 2.38×10^{15} J, giving a moment-scaled radiated energy (E_R/M_0) of 5.7×10^{-6} , somewhat low among interplate thrust events (average $E_R/M_0 \sim 1.1 \times 10^{-5}$), but not as low as observed for tsunami earthquakes with E_R/M_0 ranging from $\sim 1 \times 10^{-6}$ to 4×10^{-6} (Ye, Lay, et al., 2016).

The waveform fits are very good, with the model accounting for about 86% of the power in the observed signals (Fig. 4). The waveforms are relatively smooth and the two-subevent character of the moment rate function is reflected in the double arrivals evident in the P waves at various azimuths. Comparable waveform fits and similar slip distribution are found for models with

Figure 3. Finite-fault slip model for the M_w 7.7 mainshock in map view. Red and blue stars indicate the mainshock epicenter from the USGS-NEIC catalog and that used for the 2.5D inversion, respectively. White-dashed curves are the SLAB2 plate interface depths in 20 km increments. The white-toothed curve is the position of the trench. Global CMT focal mechanisms for events prior to the mainshock are shown in gray. Global CMT solutions for the mainshock and aftershocks are shown at the centroid locations, color-coded by centroid depth (Fig. 1c). Brown dots show aftershocks in the first 45 days. The depth below the sea surface (H) of each row of the grid is shown on the right, with the water depths (H_{water}) used in local 1D velocity model computations for each row being adapted from the regional bathymetry model and the dip angles (δ) approximated from the SLAB 2 model. The unit of both H and H_{water} is km. The overall fault representation is a 2.5D approximation of the SLAB2 model and bathymetry.

maximum rupture speed of 2.0 and 3.0 km/s, so the resolution of the bilateral rupture expansion speed is limited, but the basic depth range and slip extent are stably determined. The static stress-drop estimates for this model are 5.5 MPa for a slip-weighted estimate and 5.3 MPa for an equivalent circular model with area corresponding to the subfaults with more than 15% of the peak slip following Ye, Lay, et al. (2016).

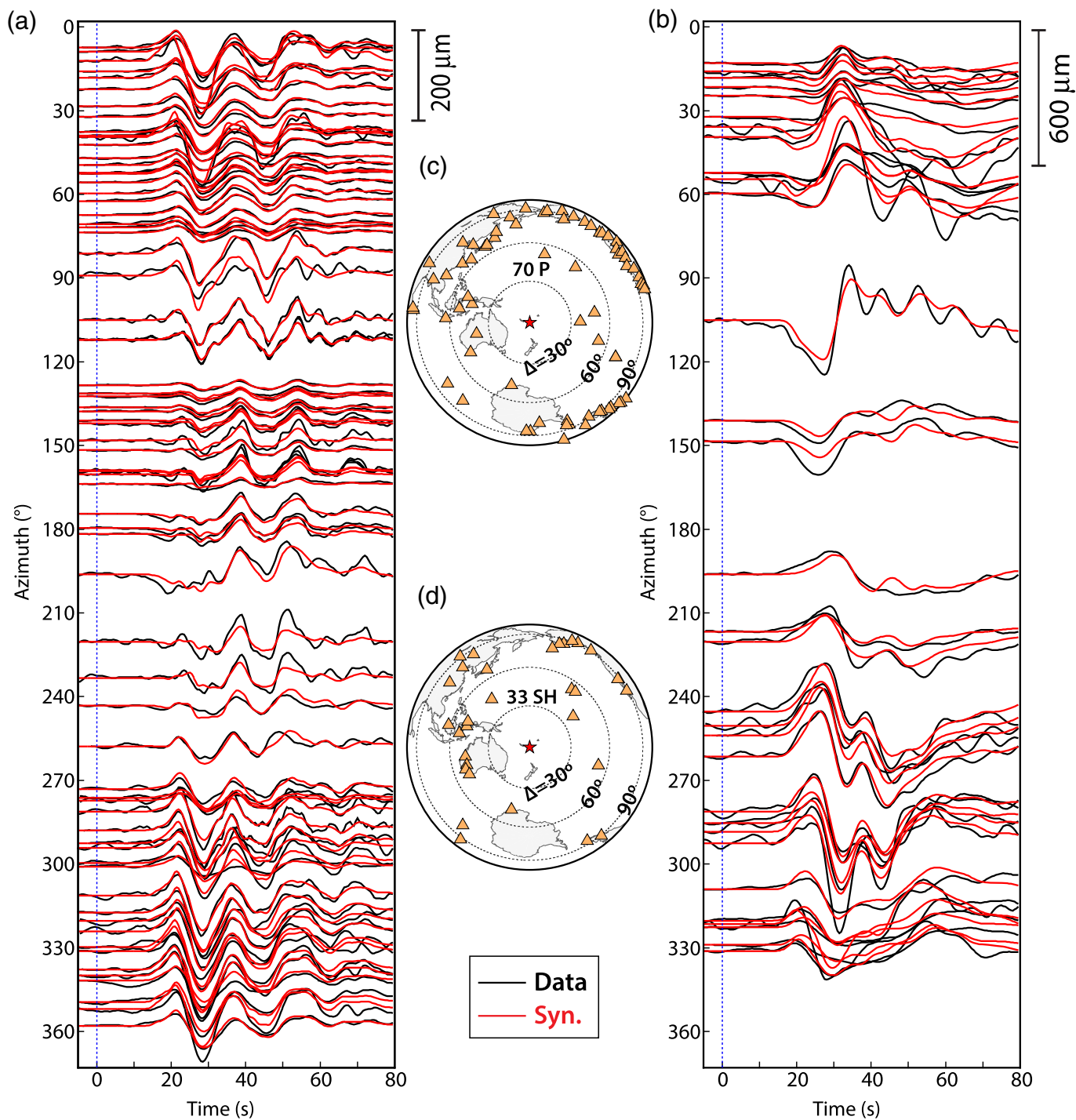


Figure 4. (a,b) Comparison of observed (black) and predicted (red) teleseismic *P* and *SH* waves shown as a function of station azimuth. (c,d) The station distributions in the stereographic projection. The red star indicates the mainshock epicenter.

Discussion

Tsunamis and coda constraints on shallow slip

Large tsunamis have seldom been generated by earthquakes in southern Vanuatu. The 28 March 1875 $M \sim 8.1$ and 1920 $M \sim 7.8$ events located well to the northwest from the 2021 sequence are among the most damaging (Sahal *et al.*, 2010;

Ioualalen *et al.*, 2017; Fig. 1a). The 2021 M_w 7.7 mainshock produced modest tsunami recorded at distant NOAA DART stations, tide gauges stations in New Caledonia and New Zealand, and New Zealand DART stations along Tonga and the southern New Hebrides. The tsunami waves at these stations are mostly less than 20 cm in amplitude, consistent with expectations given the moderate size of an event with slip of less than 4.2 m at depths from 10 to 25 km.

The up-dip extent of slip is always difficult to resolve, and is important for the strength of tsunami excitation. If significant slip extends to shallow depths close to the trench, strong water multiples (p_wP) will be excited in the deep water, giving ringing P -wave coda that will not be as strongly excited if slip is confined to greater depth (e.g., Lay *et al.*, 2019). For the M_w 7.7 mainshock, we examined azimuthally distributed P -wave coda amplitudes relative to direct P amplitudes at epicentral distances from 80° to 120° and found elevated median ratios (~ 0.79) relative to events for which no slip occurred on the shallow megathrust but with slip typically in the 20–40 km depth range (fig. 6 in Lay *et al.*, 2019). The median m_B of 7.27 for a period of 4.9 s (51 channels from 30° to 80°), and the coda magnitude m_{coda} median value of 7.11, give $m_{\text{coda}} - m_B = -0.16$, which is within the range of values for events that do have some shallow slip in figure 11 of Lay *et al.* (2019). These observations are consistent with the primary slip locating relatively shallow on the megathrust, but not as concentrated below deep water as for the uniform fault dip inversions. In the depth-varying megathrust scenario of Lay *et al.* (2012), this earthquake appears to primarily rupture Domain B (15–35 km deep), with minor penetration up into, but not total rupture, Domain A (<15 km deep).

Aftershocks and seismicity between the two large events

The USGS-NEIC distribution of seismicity prior to and after the large 2021 southern Loyalty Islands event is shown in Figure 1a. The aftershock sequence, involving 347 aftershocks with $M_w \geq 4.5$ reported by USGS-NEIC in the first 45 days, is highly productive. Globally, shallow earthquakes with M_w 7.7 on average have about 62 events in that magnitude and time interval (Ye *et al.*, 2020), and this sequence is at the upper limit of the global observed aftershock productivity distribution. Four of the aftershocks have M_w in the range 6.1–6.3, with two being thrusting events and two, including the largest event, having normal-faulting mechanisms. One hundred and nine aftershocks in the first 45 days have $M_w \geq 5.0$. Many

aftershocks are located south of the trench with the larger events involving shallow normal faulting (Figs. 1 and 4). The region of large-slip zone for the 2021 rupture has only a few overlapping Global CMT solutions from 1976 to 2020 and is located down-dip of a band of shallow thrusting mechanisms, although uncertainty in the centroid locations must be kept in mind. Prior seismicity from the USGS-NEIC catalog has shallow activity as well, but there is some overlap with the up-dip portion of the 2021 large-slip zone.

Strong activation of outer trench slope tensional ruptures in the aftershock sequence of an interplate thrust event is closely associated with shallow slip occurring on the megathrust (e.g., Wetzler *et al.*, 2017; Sladen and Trevisan, 2018; Ye *et al.*, 2021). Interaction of the stress regime in the outer rise and trench slope with the interplate earthquake cycle has long been discussed (e.g., Christensen and Ruff, 1988), and recent updates strongly support the increase in shallow tensional faulting after large interplate thrust earthquakes overall (Ye *et al.*, 2021). The basic explanation is that when the interplate boundary is locked and accumulating strain, the plate bending stress near the trench is reduced, suppressing tensional faulting. Release of the strain accumulation with megathrust rupture abruptly allows elastic bending stresses to increase, producing normal faulting seaward of the large-slip zone in the megathrust rupture. This model is generally consistent with the observations for the 2021 M_w 7.7 southeast Loyalty Islands sequence.

Strong interactions between the megathrust and intraplate environment seaward of the trench have also been observed for numerous sequences along the southern Vanuatu arc and the Loyalty Islands, northwest of the 2021 sequence. Figure 5 shows time series of the 1995, 2003–2004, and 2018 sequences, including both USGS-NEIC seismicity and Global CMT focal mechanism catalogs. They all have significant aftershock counts within the magnitude-scaled source region (white circles) for $M_w \geq 4.5$ events within 45 days of the mainshock, suggesting that these events are all more productive than the global averages for similar size mainshocks (Ye *et al.*, 2020). Together with the 2021 sequence, the southern Loyalty Islands region is found to have characteristically high aftershock productivity and unusually strong interactions between megathrust and outer trench slope activity in general.

Conclusions

The 2021 southeast Loyalty Islands interplate thrust sequence involved a very productive faulting activity with large foreshocks and many aftershocks of the M_w 7.7 mainshock. Slip

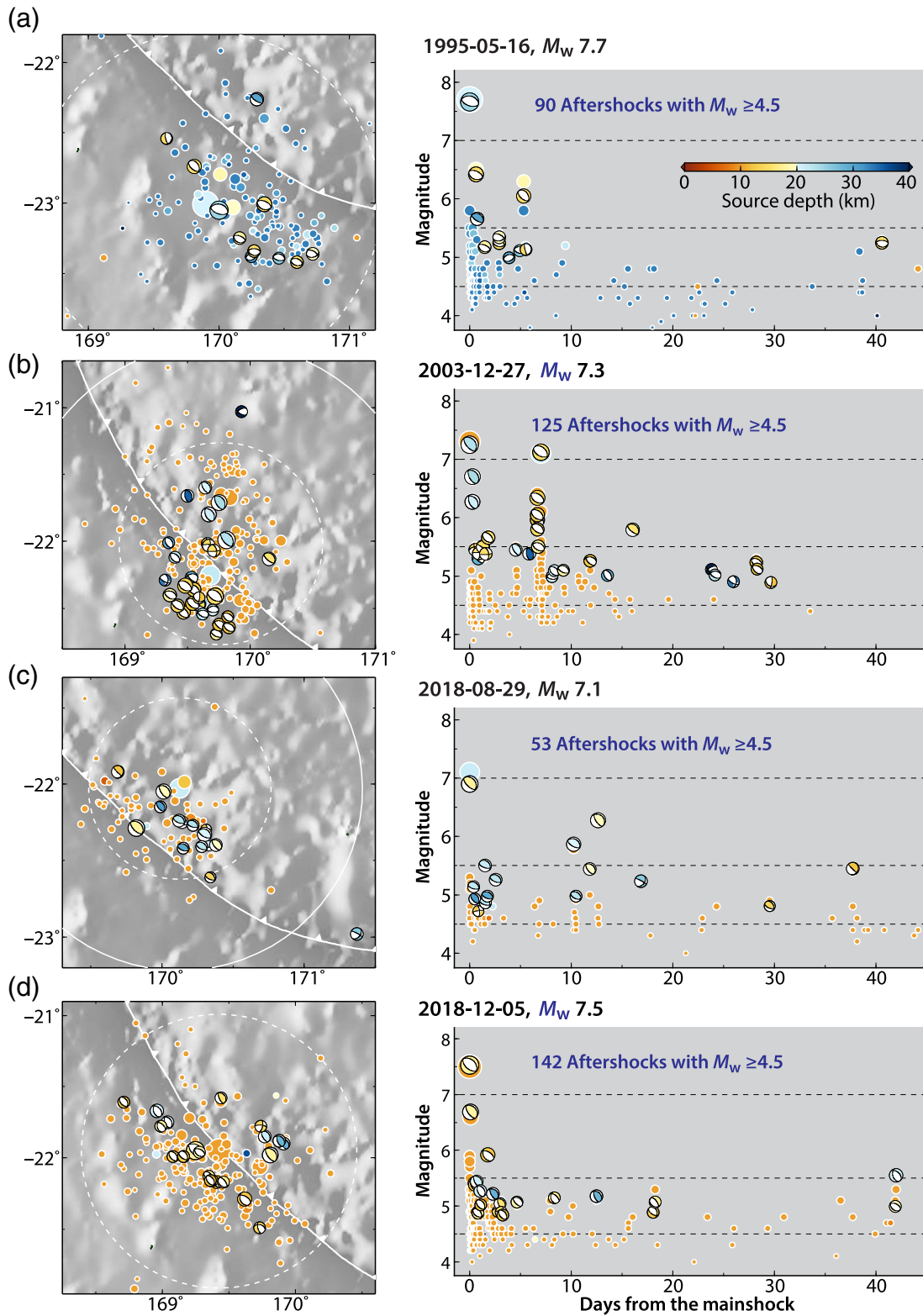


Figure 5. Large earthquake sequences along the Loyalty Islands region for events in (a) 1995 and (b) an M_w 7.0 doublet in 2003–2004, and panels (c) and (d) show two large earthquake sequences in 2018. The solid-white circle indicates the region used for aftershock counting, with the dashed

circle indicating the half-radius source zone, following [Ye et al. \(2020\)](#). USGS-NEIC aftershocks within 45 days are shown in map view and time-lines for each sequence (dots), along with Global CMT focal mechanisms.

during the mainshock was concentrated at relatively shallow depths of 10–25 km, but it does not appear that much slip occurred in the uppermost portion of the megathrust. The shallow slip generated a modest tsunami detected as far away as New Zealand, but the rupture does not appear to be as slow or as energy deficient as would characterize a tsunami earthquake. The relatively shallow concentrated slip does appear to have enhanced triggering of outer trench slope normal faulting directly seaward of the slip zone, producing several aftershocks larger than M_w 6.0 and many smaller events. This interaction between the megathrust and the intraplate environment seaward of the trench is a robust characteristic of the productive earthquake sequences along the Loyalty Islands.

Data and Resources

Body wave and surface wave recordings from global seismic stations were downloaded from the Incorporated Research Institutions for Seismology (IRIS) Data Management Center (https://ds.iris.edu/wilbert3/find_event, last accessed November 2021). Global Centroid Moment Tensor (Global CMT) solutions are from <https://www.globalcmt.org/CMTsearch.html> (last accessed November 2021). Earthquake information is based on the catalog of the National Earthquake Information Center at the U.S. Geological Survey (USGS-NEIC) (<https://earthquake.usgs.gov/earthquakes>, last accessed May 2021). The hypocenter and finite-fault information for the 10 February 2021 M_w 7.7 mainshock from the USGS-NEIC are available at <https://earthquake.usgs.gov/earthquakes/eventpage/us6000dg77/executive> (last accessed November 2021).

Data Availability Statement and Declaration

All data used in this study are openly available from the sources listed in [Data and Resources](#).

Declaration of Competing Interests

The authors acknowledge there are no conflicts of interest recorded.

Acknowledgments

The authors thank Editor Keith Koper, Associate Editor Ruth Harris, and two anonymous reviewers for their helpful comments on this article. Lingling Ye's and Xiaofei Chen's earthquake study are supported by National Natural Science Foundation of China (41874056, 41790465, and U1901602). Thorne Lay's research on earthquake processes is supported by National Science Foundation Grant EAR1802364.

References

- Calmant, S., B. Pelletier, and P. Lebellegard (2003). New insights on the tectonics along the New Hebrides subduction zone based on GPS results, *J. Geophys. Res.* **108**, 2319.
- Christensen, D. H., and L. J. Ruff (1988). Seismic coupling and outer rise earthquakes, *J. Geophys. Res.* **93**, 13,421–13,444.
- Cleveland, K. M., C. J. Ammon, and T. Lay (2014). Large earthquake processes in the northern Vanuatu subduction zone, *J. Geophys. Res.* **119**, 8866–8883.
- DeMets, C., R. G. Gordon, and D. F. Argus (2010). Geologically current plate motions, *Geophys. J. Int.* **181**, 1–80.
- Fan, F., L. Ye, H. Kanamori, and T. Lay (2021). Responding to media inquiries about earthquake triggering interactions, *Seismol. Res. Lett.* **92**, no. 5, 3035–3045.
- Hartzell, S. H., and T. H. Heaton (1983). Inversion of strong ground motion and teleseismic waveform data for the fault rupture history of the 1979 Imperial Valley California earthquake, *Bull. Seismol. Soc. Am.* **73**, 1553–1583.
- Hayes, G. P., K. P. Furlong, H. M. Benz, and M. W. Heerman (2014). Triggered aseismic slip adjacent to the 6 February 2013 M_w 8.0 Santa Cruz Islands megathrust earthquake, *Earth Planet. Sci. Lett.* **388**, 265–272.
- Hayes, G. P., G. L. Moore, D. E. Portner, M. Hearne, H. Flamme, M. Furtney, and G. M. Smoczyk (2018). Slab 2, a comprehensive subduction zone geometry model, *Science* **362**, 58–61.
- Ioualalen, M., B. Pelletier, and G. Solis Gordillo (2017). Investigating the March 28th 1875 and the September 20th 1920 earthquakes/tsunamis of the southern Vanuatu arc, offshore Loyalty Islands, New Caledonia, *Tectonophysics* **709**, 20–38.
- Kanamori, H., and L. Rivera (2008). Source inversion of W phase: speeding up seismic tsunami warning, *Geophys. J. Int.* **175**, 222–238.
- Kikuchi, M., and H. Kanamori (1991). Inversion of complex body waves-III, *Bull. Seismol. Soc. Am.* **81**, 2335–2350.
- Laske, G., G. Masters, Z. Ma, and M. Pasyanos (2013). Update on CRUST1.0 – a 1-degree global model of Earth's crust, *Geophys. Res. Abstr.* **15**, Abstract EGU2013-2658.
- Lay, T., H. Kanamori, C. J. Ammon, K. D. Koper, A. R. Hutko, L. Ye, H. Yue, and T. M. Rushing (2012). Depth-varying rupture properties of subduction zone megathrust faults, *J. Geophys. Res.* **117**, B04311.
- Lay, T., C. Liu, and H. Kanamori (2019). Enhancing tsunami warning using P wave coda, *J. Geophys. Res.* **124**, 10,583–10,609.
- Lay, T., L. Ye, H. Kanamori, Y. Yamazaki, K. F. Cheung, and C. J. Ammon (2013). The February 6, 2013 M_w 8.0 Santa Cruz Islands earthquake and tsunami, *Tectonophysics* **608**, 1109–1121.
- Lister, G. S., L. T. White, S. Hart, and M. A. Forster (2012). Ripping and tearing the rolling-back New Hebrides slab, *Aust. J. Earth Sci.* **59**, 899–911.
- Louat, R., and B. Pelletier (1989). Seismotectonics and present-day relative plate motion in the New Hebrides-North Fiji basin region, *Tectonophysics* **167**, 41–55.
- McCann, W. R., S. P. Nishenko, L. R. Sykes, and J. Krause (1979). Seismic gaps and plate tectonics: Seismic potential for major boundaries, *Pure Appl. Geophys.* **117**, 1082–1147.

- Monzier, M., P. Maillet, J. Foyo Herrera, R. Louat, F. Missegue, and B. Pontoise (1984). The termination of the southern New Hebrides subduction zone (southwestern Pacific), *Tectonophysics* **101**, 177–184.
- Nishenko, S. P. (1991). Circum-Pacific seismic potential: 1989–1999, *Pure Appl. Geophys.* **135**, 169–259.
- Sahal, A., B. Pelletier, J. Chatelier, F. Lavigne, and F. Schindel  (2010). A catalog of tsunamis in New Caledonia from 28 March 1875 to 30 September 2009, *C. R. Geosci.* **342**, 434–447.
- Sladen, A., and J. Trevisan (2018). Shallow megathrust earthquake ruptures betrayed by their outer-trench aftershocks signature, *Earth Planet. Sci. Lett.* **483**, 105–113.
- Vidale, J., and H. Kanamori (1983). The October 1980 earthquake sequence near the New Hebrides, *Geophys. Res. Lett.* **10**, 1137–1140.
- Wetzler, N., T. Lay, E. E. Brodsky, and H. Kanamori (2017). Rupture-depth-varying seismicity patterns for major and great ($M_W \geq 7.0$) megathrust ruptures, *Geophys. Res. Lett.* **44**, 9663–9671.
- Ye, L., H. Kanamori, J. P. Avouac, L. Li, K. F. Cheung, and T. Lay (2016). The 16 April 2016, M_w 7.8 (M_s 7.5) Ecuador earthquake: a quasi-repeat of the 1942 M_s 7.5 earthquake and partial re-rupture of the 1906 M_s 8.6 Colombia-Ecuador earthquake, *Earth Planet. Sci. Lett.* **458**, 248–258.
- Ye, L., T. Lay, and H. Kanamori (2020). Anomalously low aftershock productivity of the 2019 M_W 8.0 energetic intermediate-depth faulting beneath Peru, *Earth Planet. Sci. Lett.* **549**, 116528.
- Ye, L., T. Lay, and H. Kanamori (2021). The 25 March 2020 M_W 7.5 Paramushir, northern Kuril Islands earthquake and major ($M_W \geq 7.0$) near-trench intraplate compressional faulting, *Earth Planet. Sci. Lett.* **556**, 115728.
- Ye, L., T. Lay, H. Kanamori, and L. Rivera (2016). Rupture characteristics of major and great ($M_W \geq 7.0$) megathrust earthquakes from 1990–2015: 1. Source parameter scaling relationships, *J. Geophys. Res.* **121**, 826–844.

Manuscript received 27 September 2021

Published online 1 December 2021